In Situ Growth of Lead-Free Double Perovskite Micron Sheets in Polymethyl Methacrylate for X-Ray Imaging

Jindou Shi, Zeyu Wang,* Luxia Xu, Junnan Wang, Zheyuan Da, Chen Zhang, Yongqiang Ji, Qing Yao, Youlong Xu, Nikolai V. Gaponenko, Jinshou Tian, and Minqiang Wang

Pb-free double-perovskite (DP) scintillators are highly promising candidates for X-ray imaging because of their superior optoelectronic properties, low toxicity, and high stability. However, practical applications require Pb-free DP crystals to be ground and mixed with polymers to produce scintillator films. Grinding can compromise film uniformity and optical properties, thereby affecting imaging resolution. In this study, an in situ fabrication strategy is proposed to facilitate the crystalline growth of Pb-free $Cs_2AgIn_xBi_{1-x}Cl_6$ micron sheets in polymethyl methacrylate in a single step. By adjusting the In^{3+}/Bi^{3+} ratio, $Cs_2AgIn_{0.9}Bi_{0.1}Cl_6$/PMMA composite films (CFs) with excellent scintillation properties are obtained, including a light yield of up to 32000 photons per MeV and an X-ray detection limit of 87 $nGy_{air}s^{-1}$. This strategy also enabled the production of large $Cs_2AgIn_{0.9}Bi_{0.1}Cl_6$/PMMA CFs, which demonstrated favorable flexibility and stability, fabricating products with advanced eligibility for commercial applications. The CFs exhibited outstanding performances in X-ray imaging, producing high-resolution structures and providing a new avenue for the development of Pb-free DP materials in fields such as medical imaging and safety detection.

1. Introduction

Recently, scintillator materials have been extensively applied in medical imaging, industrial nondestructive detection, safety detection, and radiation monitoring owing to their ability to transform high-energy X-ray photons into low-energy visible photons.[1–7] However, there remain significant challenges despite the development of numerous inorganic scintillators such as single crystals, oxy-halides, and inorganic/hybrid halides.[8–11] These include the high-temperature sintering of single crystals, moisture absorption by halides, and inadequate stability and Pb toxicity of Pb halide perovskites, which potentially induce high energy costs and environmental pollution, significantly restricting the commercialization of these scintillator materials.[12–15] Therefore, it is imperative to explore scintillator materials that provide low energy cost, enhanced stability, and environmental friendliness.

Pb-free double perovskite (DP) crystals, $Cs_2B^+B^{3+}X_6$ (B^+: Ag^+ and Na^+; B^{3+}: In^{3+}, Bi^{3+}, and Sb^{3+}; $X = Cl$ and Br), are regarded as promising candidates for new-generation scintillator materials. These crystals feature corner-sharing X^- anions that link alternating $[B^+X_6]^{5-}$ and $[B^{3+}X_6]^{3-}$ octahedra, forming stabilized cubic structures that replace highly polluting Pb ions.[16–20] Zhang et al. prepared $Cs_2Na_{0.9}Ag_{0.1}LuCl_6:Dy^{3+}$ DP single crystals co-doped with Dy^{3+} and Ag^+ ions using a hydrothermal method, followed by mixing the ground single crystals with an acrylic pressure-sensitive adhesive to prepare a flexible scintillator film that can be used in the X-ray imaging of nonplanar and irregular objects.[21] Varnakavi et al. synthesized Mn (II)-doped $Cs_2NaBiCl_6$ DP nanocrystals (NCs) using a modified thermal injection method. These NCs were mixed with polymethyl methacrylate (PMMA) to fabricate an orange-emitting $Cs_2NaBiCl_6$:4.04%Mn@PMMA film that exhibited favorable X-ray imaging properties and excellent stability under prolonged exposure to X-rays.[22] Generally, bulk Pb-free DP single crystals or NCs are initially grown and subsequently mixed with a polymer to produce Pb-free DP scintillator films.[23–29] However, this method is constrained by the low yield of DP crystals and uneven powder distribution; therefore, the production of uniform, large scintillator films that directly impact the imaging resolution is challenging.[30] Furthermore,

J. Shi, J. Wang, Z. Da, C. Zhang, Y. Ji, Q. Yao, Y. Xu, M. Wang
Electronic Materials Research Laboratory
Key Laboratory of the Ministry of Education International Center for Dielectric Research&Shannxi Engineering Research Center of Advanced Energy Materials and Devices
Xi'an Jiaotong University
Xi'an 710049, China

Z. Wang
Frontier Institute of Science and Technology (FIST), and Micro- and Nano-technology Research Center of State Key Laboratory for Manufacturing Systems Engineering
Xi'an Jiaotong University
Xi'an 710049, China
E-mail: zeyu.wang@xjtu.edu.cn

L. Xu, J. Tian
Xi'an Institute of Optics and Precision Mechanics
Xi'an, Shaanxi 710119, P. R. China

N. V. Gaponenko
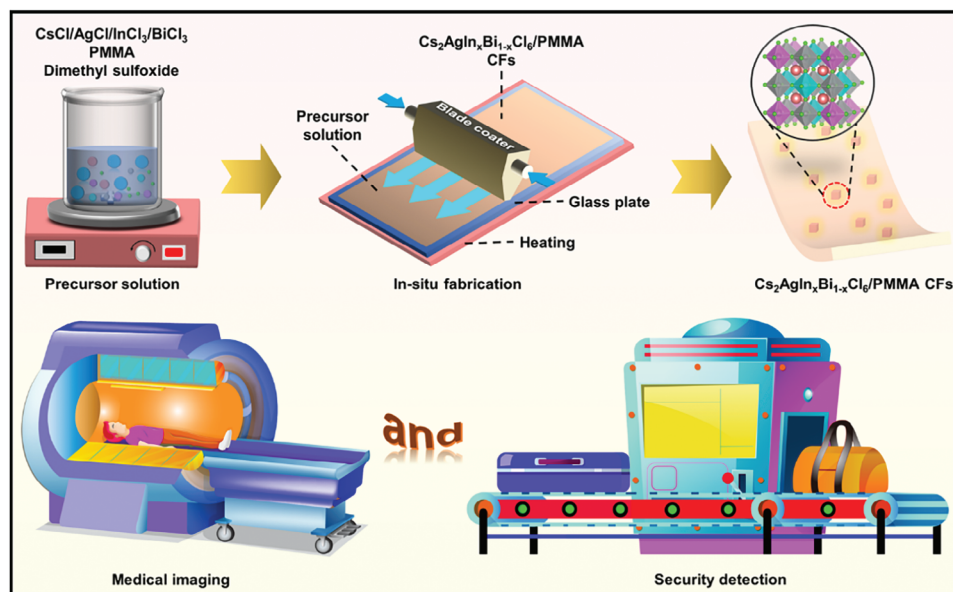Belarusian State University of Informatics and Radioelectronics
P. Browki 6, Minsk 220013, Belarus

Figure 1. Schematic of the in situ fabrication of large-sized $Cs_2AgIn_xBi_{1-x}Cl_6$/PMMA CFs as well as their potential application in X-ray imaging.

the original optical properties of DP single crystals can be compromised during grinding, thereby hindering their further development in practical scintillation applications.[27] Consequently, there is a pressing need for a preparation technology that is efficient, cost-effective, and capable of producing large scintillator films that can further the development of Pb-free DP scintillator materials.

In this study, a convenient and lower-energy-cost in situ fabrication strategy, based on a previous study, was proposed for obtaining environmentally friendly large-sized Pb-free DP scintillator films by optimizing the crystallization temperature and modulating the transmittance.[17] All raw materials were dissolved in dimethyl sulfoxide (DMSO), and $Cs_2AgInCl_6$ micron sheets (MSs) were grown directly in situ within PMMA using a knife coating and annealing process, which facilitated the formation of large and uniform $Cs_2AgInCl_6$/PMMA composite films (CFs) in a single step (**Figure 1**). Subsequently, in situ doping of Bi^{3+} in $Cs_2AgInCl_6$/PMMA CFs was accomplished by adjusting the initial feed ratio, significantly enhancing the corresponding optical properties and laying the foundation for downstream X-ray detection. The $Cs_2AgIn_{0.9}Bi_{0.1}Cl_6$/PMMA CFs exhibited exceptional optical properties, with an X-ray detection limit of 87 $nGy_{air}s^{-1}$, surpassing the thresholds required for practical medical imaging applications. Additionally, large-scale $Cs_2AgIn_{0.9}Bi_{0.1}Cl_6$/PMMA CFs demonstrated excellent flexibility and stability under X-ray irradiation, fostering significant advancements in commercial sectors, such as medical imaging and security detection.

2. Results and Discussion

Using an in situ preparation strategy, $Cs_2AgIn_xBi_{1-x}Cl_6$/PMMA CFs were fabricated via the one-step growth of $Cs_2AgIn_xBi_{1-x}Cl_6$ crystals in polymer PMMA. Subsequently, X-ray diffraction (XRD), scanning electron microscopy (SEM), and energy-dispersive X-ray spectroscopy (EDS) were used to investigate the crystal structure and micromorphology of $Cs_2AgIn_xBi_{1-x}Cl_6$ in

the CFs. Highly crystalline Pb-free DP crystal diffraction peaks were observed in all samples of the $Cs_2AgIn_xBi_{1-x}Cl_6$/PMMA CFs with varying contents of In^{3+}. Diffraction peaks of highly crystalline Pb-free DP crystals were detected in the samples with trace Bi^{3+} doping, which corresponded to the pure bulk $Cs_2AgInCl_6$ reference (ICSD: 257115). However, the DP crystals in the $Cs_2AgIn_xBi_{1-x}Cl_6$/PMMA CFs gradually converted into $Cs_2AgBiCl_6$ (ICSD: 291598) as the ratio of Bi^{3+}/In^{3+} increased; additionally, a significant change in crystal structure was significant (**Figure 2a**, left). A broad, but weak diffraction peak was observed at 15° in the XRD patterns of all CFs, which was consistent with the XRD pattern of the amorphous pure PMMA film (Figure S1, Supporting Information). This confirmed that the in situ growth of $Cs_2AgIn_xBi_{1-x}Cl_6$ within PMMA was completed. Moreover, the diffraction peaks of the DP crystals in $Cs_2AgIn_xBi_{1-x}Cl_6$/PMMA CFs shifted to a lower 2θ angle after the introduction of Bi^{3+} in the 23°–25° range (Figure 2a, right). This originated from the lattice expansion triggered by the replacement of the smaller ionic radius of In^{3+} (94 pm) with the larger radius of Bi^{3+} (117 pm); a similar phenomenon was previously observed in other Pb-free DP materials.[31,32] The microscopic morphology of various CFs was observed using SEM. The surface of the pure PMMA film was smooth and no crystals were observed under the same fabrication conditions (Figure 2b). Conversely, many sheet-like $Cs_2AgInCl_6$ crystals were embedded in $Cs_2AgInCl_6$/PMMA CFs, with an average size of ≈80 µm (Figure 2c). The $Cs_2AgInCl_6$ MSs in the $Cs_2AgInCl_6$/PMMA CFs were quadrilateral in shape with irregular edges and holes in the center. This shape was attributed to uneven PMMA shrinkage during thermal annealing (Figure 2d).[17] Furthermore, the darker coloration was due to the PMMA polymer on the surface of $Cs_2AgIn_xBi_{1-x}Cl_6$, and the substrate color could be observed through the polymer owing to its high transmittance. The surface of the $Cs_2AgInCl_6$ MSs was smooth and no other attached crystals were observed (Figure 2e), suggesting that micrometer-scale $Cs_2AgInCl_6$ was successfully grown in
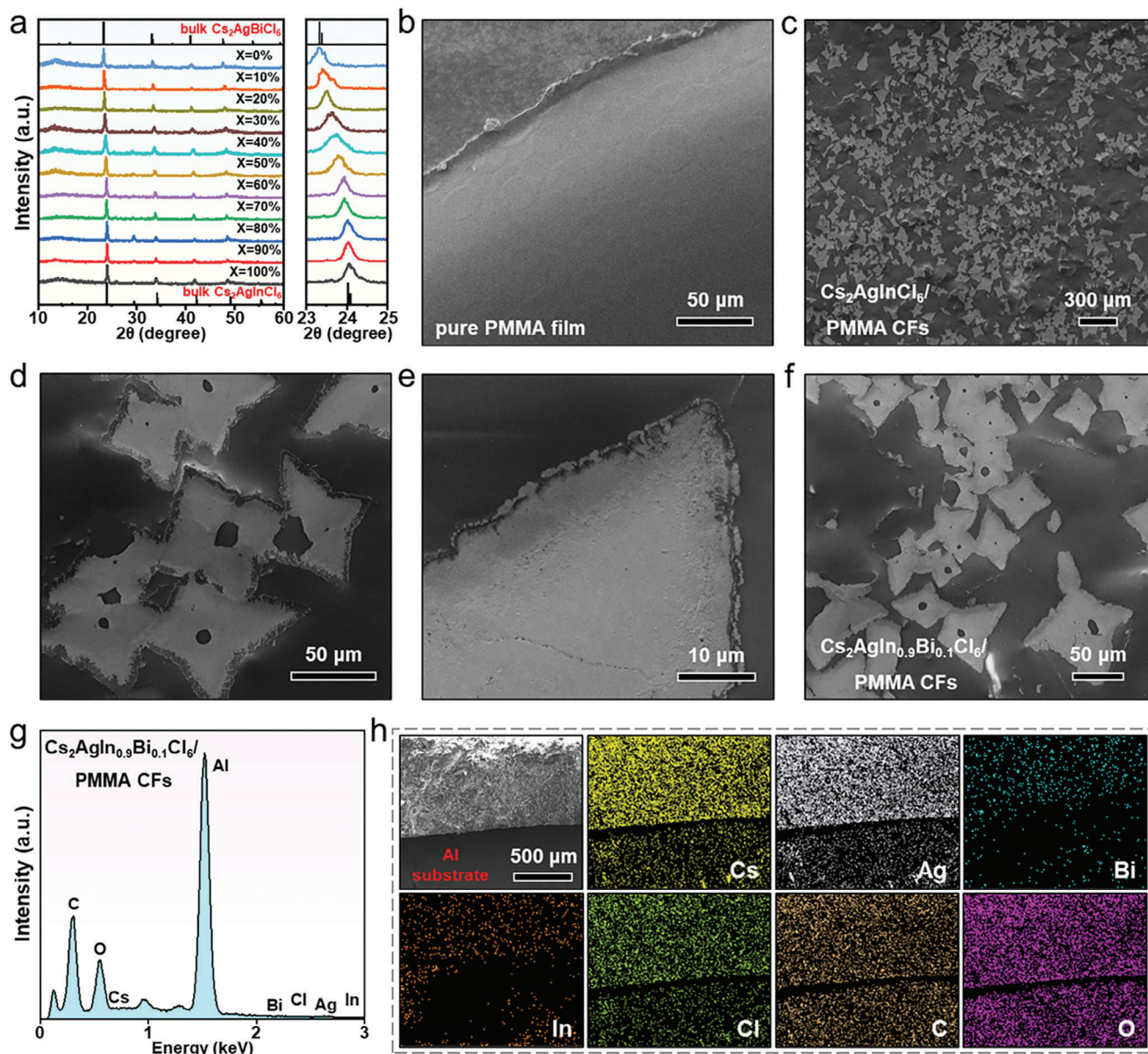
**ADVANCED
SCIENCE NEWS**

www.advancedsciencenews.com

**ADVANCED
OPTICAL
MATERIALS**

www.advopticalmat.de

Figure 2. a) XRD patterns of $Cs_2AgIn_xBi_{1-x}Cl_6$/PMMA CFs with varying In^{3+} content. The lowest line corresponds to a pure bulk $Cs_2AgInCl_6$ (ICSD: 257115), whereas the highest line corresponds to a pure bulk $Cs_2AgBiCl_6$ (ICSD: 291598). Magnification of the XRD patterns in the 23°–25° range. SEM images of b) pure PMMA film, c) $Cs_2AgInCl_6$/PMMA CFs, d,e) magnified $Cs_2AgInCl_6$/PMMA CFs, and f) $Cs_2AgIn_{0.9}Bi_{0.1}Cl_6$/PMMA CFs. g) EDS spectrum and h) elemental mapping of $Cs_2AgIn_{0.9}Bi_{0.1}Cl_6$/PMMA CFs.

situ in PMMA. Subsequently, no change in the morphology of $Cs_2AgIn_{0.9}Bi_{0.1}Cl_6$ in CFs was observed after Bi^{3+} in situ doping. The sheet retained its original micrometer shape, and no other products were observed (Figure 2f) The $Cs_2AgIn_xBi_{1-x}Cl_6$/PMMA CFs with different doping ratios (X = 80–0%) also maintained the same morphology (Figure S2a–i, Supporting Information), further confirming that this in situ preparation strategy facilitated Bi^{3+} incorporation into the crystal lattice of $Cs_2AgInCl_6$. Finally, all elements were detected in the EDS spectrum analysis of the $Cs_2AgIn_{0.9}Bi_{0.1}Cl_6$/PMMA CFs (Figure 2g). The content of Al, which originated from the substrate, was highest, and the corresponding elemental mapping indicated that the

constituent elements of the CFs were uniformly distributed (Figure 2h), closely reflecting the formation of alloying MSs in PMMA. Therefore, this in situ preparation method can fabricate $Cs_2AgIn_xBi_{1-x}Cl_6$/PMMA CFs in one step, thereby simplifying the production process and making it more suitable for large-scale commercial development.

The optical properties of the $Cs_2AgIn_xBi_{1-x}Cl_6$/PMMA CFs with varying In^{3+} contents were investigated to improve their suitability for development in the future optoelectronics market. The pure PMMA film exhibited high transmittance in the UV–vis region (Figure S3a, Supporting Information); therefore, the $Cs_2AgIn_xBi_{1-x}Cl_6$ in CFs effectively absorbed the external

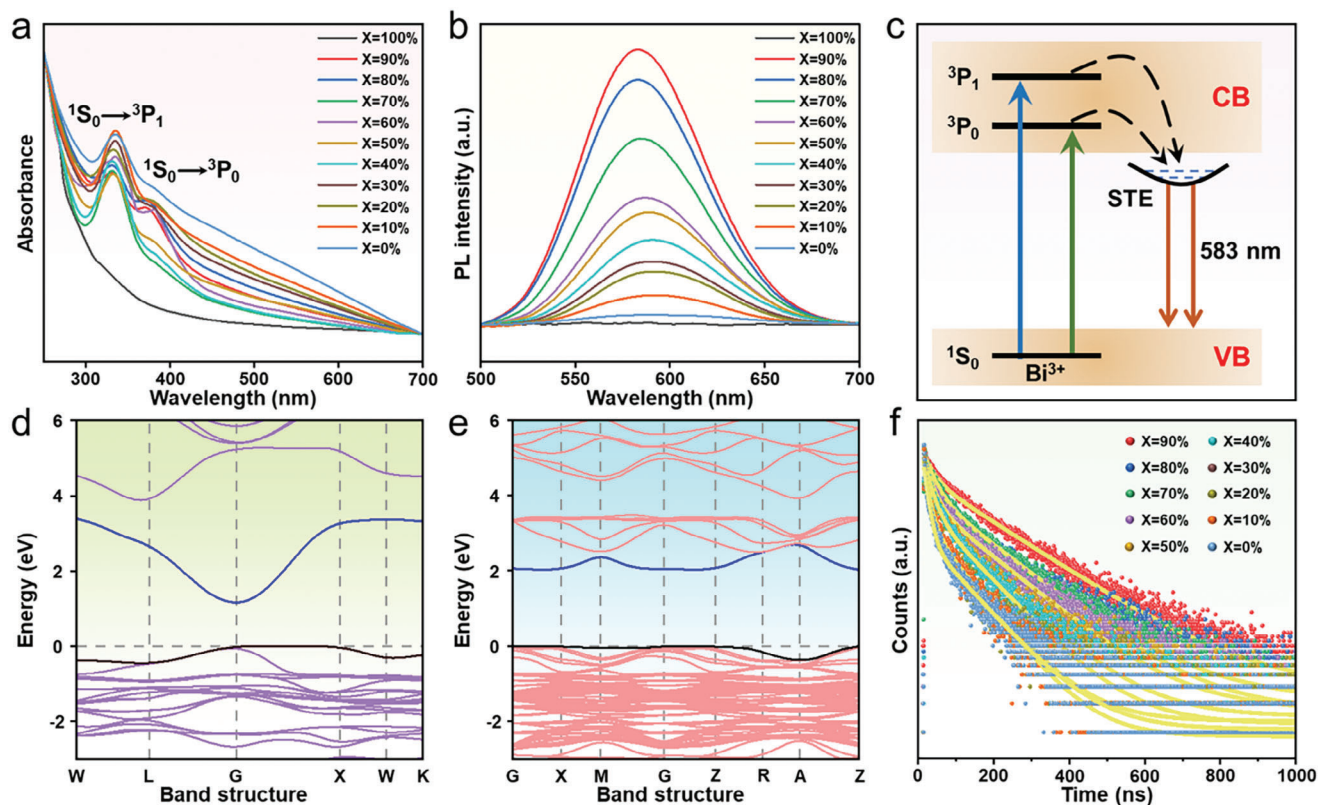**Figure 3.** a) Absorbance and b) PL spectra of $Cs_2AgIn_xBi_{1-x}Cl_6$/PMMA CFs with varying In^{3+} content. c) Energy-level diagram of $Cs_2AgIn_{0.9}Bi_{0.1}Cl_6$/PMMA CFs and the PL mechanism (CB, conduction band; VB, valence band; STE, self-trapped exciton state). Electronic band gap structure of d) $Cs_2AgInCl_6$ and e) $Cs_2AgIn_{0.75}Bi_{0.25}Cl_6$. f) Time-resolved PL spectra and fitted curves for CFs with varying In^{3+} content.

excitation energy and emitted bright fluorescence without shielding by the surface polymer layer. Furthermore, no significant peaks were detected in the UV–vis region of the absorbance spectra of $Cs_2AgIn_xBi_{1-x}Cl_6$/PMMA CFs with varying In^{3+} contents (**Figure 3a**). These CFs exhibited weaker light absorption coefficients around their bandgap, resulting in the absorbance of a quantity of excitation energy by $Cs_2AgInCl_6$ that was insufficient for the support of fluorescence emission.[33,34] Simultaneously, no significant fluorescence emission peak was observed in the $Cs_2AgInCl_6$/PMMA CFs under 365 nm UV irradiation (Figure 3b), and their PL spectra were consistent with that of the pure PMMA film (Figure S3b, Supporting Information). This suggested that $Cs_2AgInCl_6$/PMMA CFs could not be further developed in the field of optical lighting. Fortunately, the two distinct absorption peaks in $Cs_2AgIn_xBi_{1-x}Cl_6$/PMMA CFs (X = 80–0%) were accompanied by the doping of Bi^{3+} (Figure 3a), which was attributed to the s→p orbital transition of the $[BiCl_6]^{3-}$ octahedra.[35] The exciton absorption peak at 332 nm originated from the spin-forbidden $^1S_0\rightarrow^3P_1$ transition, whereas the weaker absorption peak at 378 nm was assigned to the spin-forbidden $^1S_0\rightarrow^3P_0$ transition. the intensity of the peak at 378 nm was mainly attributed to the spin and parity forbidden nature of the transition.[31,36] Simultaneously, a weak redshift was observed at the absorption edge of the $Cs_2AgIn_xBi_{1-x}Cl_6$/PMMA CFs with continued Bi^{3+} doping (Figure S4a, Supporting Information). The change in the

bandgap (Eg) values was calculated using tac plots, which showed that the bandgap of the $Cs_2AgIn_xBi_{1-x}Cl_6$/PMMA CFs decreased monotonically as In^{3+} was reduced (Figure S4b, Supporting Information); a similar phenomenon was observed for the $Cs_2AgIn_xBi_{1-x}Cl_6$ NCs.[34,37] In contrast, a broad fluorescence emission peak at 580 nm was observed in all PL spectra of the $Cs_2AgIn_xBi_{1-x}Cl_6$/PMMA CFs (X = 90–0%) (Figure 3b). This peak was attributed to the breaking of the forbidden transition of In^{3+} induced by Bi^{3+}, which enhanced the absorption of the transition and enabled more energy to be transferred to the self-trapped exciton (STE) state, resulting in the emission of bright orange light by radiative recombination (Figure 3c).[32,34] Further doping with Bi^{3+} reduced the PL intensity of the $Cs_2AgIn_xBi_{1-x}Cl_6$/PMMA CFs (Figure 3b) from 72.1% to 8.2% (Figure S5a, Supporting Information). This phenomenon can be explained by ionic composite engineering, which transforms $Cs_2AgIn_xBi_{1-x}Cl_6$ from a direct bandgap to an indirect bandgap, resulting in an increased number of trap states.[37] The transformation of the electronic structures of pure-phase $Cs_2AgInCl_6$ and marginally doped $Cs_2AgIn_{0.75}Bi_{0.25}Cl_6$ was investigated using Perdew–Burke–Ernzerhof (PBE)-DFT calculations (Figure 3d,e). The valence band maximum (VBM) and conduction band minimum (CBM) of the pure-phase $Cs_2AgInCl_6$ were simultaneously located at the G-point, exhibiting a standard direct bandgap structure (Figure 3d); the density-of-states function showed that the VBM consisted of In-p, Ag-d, and

ADVANCED
SCIENCE NEWS

www.advancedsciencenews.com

ADVANCED
OPTICAL
MATERIALS

www.advopticalmat.de

Cl-p orbitals, and the CBM consisted of In-s, Ag-s, and Cl-p orbitals (Figure S6a, Supporting Information). Unfortunately, the optical transition between the band-edge states at the G point was forbidden by parity, causing $Cs_2AgInCl_6$ to be unable to absorb sufficient energy for complete fluorescence emission, which was consistent with its PL properties (Figure 3b).[38,39] Thereafter, $Cs_2AgIn_{0.75}Bi_{0.25}Cl_6$ with a low quantity of Bi^{3+} doping exhibited a direct band gap at the G point (Figure 3e), with a VBM consisting of Ag-d, In-p, Bi-s and Cl-p orbitals, and a CBM consisting of Ag-s, In-s, Bi-p, and Cl-p orbitals (Figure S6b, Supporting Information). Although the optical transition of $Cs_2AgIn_{0.75}Bi_{0.25}Cl_6$ at the G point was also forbidden, Bi^{3+} doping introduced the s→p direct transition, which was able to break this parity prohibition and facilitate the absorption enhancement; therefore, the relaxation of electrons and holes under forbidden photoexcitation emitting orange light was observed. However, with a further increase in the Bi^{3+} content, the VBM of $Cs_2AgIn_{0.5}Bi_{0.5}Cl_6$ shifted to the Q point, whereas the CBM was located at the G point, which is a typical indirect band gap (Figure S6c, Supporting Information). The VBM of $Cs_2AgIn_{0.5}Bi_{0.5}Cl_6$ consisted of Ag-d, In-p, Bi-s, and Cl-p orbitals, whereas its CBM consisted of Ag-s, In-s, Bi-p, and Cl-p orbitals (Figure S6d, Supporting Information), which coincided with the orbital constitution of $Cs_2AgIn_{0.75}Bi_{0.25}Cl_6$. However, excess Bi^{3+} resulted in the mixing of the Ag and Bi frontier orbitals in the VBM and CBM of $Cs_2AgIn_{0.5}Bi_{0.5}Cl_6$, such that the Ag-Bi DP crystals exhibited an indirect bandgap structure. This resulted in the absence of the fluorescence property.[34,40] Additionally, a redshift in the PL peak of the $Cs_2AgIn_xBi_{1-x}Cl_6$/PMMA CFs from 582 to 591 nm was observed as the In^{3+} content decreased (Figure S5b, Supporting Information) because of the gradual narrowing of the bandgap due to Bi^{3+} substitution for In^{3+}; this change was consistent with their absorbance spectra. Therefore, trace doping with Bi^{3+} caused $Cs_2AgInCl_6$ to emit a bright orange light, whereas excessive doping caused fluorescence quenching. Thus, $Cs_2AgIn_{0.9}Bi_{0.1}Cl_6$/PMMA CFs have shown outstanding optical properties, making them more suitable for the development of the optoelectronics market. Subsequently, the influence of Bi^{3+} doping on the carrier dynamics of the $Cs_2AgIn_xBi_{1-x}Cl_6$/PMMA CFs was investigated by recording the time-resolved PL spectra of the CFs (Figure 3f). The fitting results indicated that the PL decays of all CFs can be fitted using a bi-exponential function (Figure 3f; Table S1, Supporting Information), where the short-lifetime component of the PL decay (τ_1) was assigned to the non-radiative recombination, and the intermediate-lifetime component (τ_2) was assigned to the radiative recombination.[17,41,42] The nonradiative recombination ratio (A_1) of the $Cs_2AgIn_xBi_{1-x}Cl_6$/PMMA CFs gradually increased, whereas the radiative recombination ratio gradually decreased (A_2) with a continual increase in Bi^{3+} doping, which was consistent with the changes in their PL spectra (Figure 3b). The $Cs_2AgIn_{0.9}Bi_{0.1}Cl_6$/PMMA CFs exhibited outstanding optical properties, making them ideal for subsequent scintillation application studies.

Recently, the excellent stability and optical properties of Pb-free DP crystals have attracted widespread attention in fields such as X-ray detection and imaging. In this study, in situ, fabricated $Cs_2AgIn_{0.9}Bi_{0.1}Cl_6$/PMMA CFs with excellent optical properties and a convenient production process showed potential for future applications in the field of X-ray imaging. The X-ray absorption spectra of $Cs_2AgInCl_6$ and $Cs_2AgIn_{0.9}Bi_{0.1}Cl_6$ were simulated according to the XCOM photon cross-section database and compared with the X-ray absorption coefficients of some conventional semiconductors (CsI:TI, CdTe, LuAG:Ce) under different photon energies (**Figure 4a**). These compounds exhibited the same excellent ability to absorb radioactive particles as the conventional semiconductors. Subsequently, the radioluminescence (RL) spectra of all CFs were detected under the same conditions (X-ray dose rate of 20 $\mu Gy_{air}s^{-1}$, 50 keV) to further assess the scintillating performance of $Cs_2AgIn_xBi_{1-x}Cl_6$/PMMA CFs (Figure 4b). The RL spectra of the $Cs_2AgIn_xBi_{1-x}Cl_6$/PMMA CFs were similar to their PL spectra (Figure 3b) as both exhibited a broad orange emission peak at 580 nm, implying that the same radiative recombination channel was present for the $Cs_2AgIn_xBi_{1-x}Cl_6$/PMMA CFs under X-ray and 365 nm UV excitation, such that the RL intensity of the $Cs_2AgIn_{0.9}Bi_{0.1}Cl_6$/PMMA CFs remained ahead. Subsequently, the light yield of $Cs_2AgIn_xBi_{1-x}Cl_6$/PMMA CFs was calculated with a commercial scintillator (LuAG:Ce 25000 photons per MeV) as the reference to assess the scintillation performance of $Cs_2AgIn_xBi_{1-x}Cl_6$/PMMA CFs (Figure S7a, Supporting Information). The light yield of the $Cs_2AgIn_{0.9}Bi_{0.1}Cl_6$/PMMA CFs was as high as 32000 photons per MeV, whereas that of the $Cs_2AgBiCl_6$/PMMA CFs decayed to 4800 photons per MeV (Figure S7b, Supporting Information). Thereafter, the luminescence mechanism of the $Cs_2AgIn_{0.9}Bi_{0.1}Cl_6$/PMMA CFs under X-ray excitation was analyzed. This mechanism primarily consisted of three important stages: conversion, transportation, and scintillation (Figure 4c). High-energy X-rays were initially absorbed by heavy atoms (Cs, Ag, In, and Bi) in the lattice of $Cs_2AgIn_{0.9}Bi_{0.1}Cl_6$, ejecting high-energy carriers via the photoelectric and Compton scattering effects. Subsequently, the high-energy electrons and holes lost energy during thermalization and were transported to the conduction and valence bands of $Cs_2AgIn_{0.9}Bi_{0.1}Cl_6$, respectively. The luminescent center continuously traps a large number of electrons and holes, generating scintillating light through radiative transitions.[22,30] Moreover, the RL spectra of $Cs_2AgIn_{0.9}Bi_{0.1}Cl_6$/PMMA CFs at varying X-ray dose rates (2–24 $\mu Gy_{air}s^{-1}$) were collected (Figure 4d), and their corresponding RL intensities increased with the radiation dose, indicating a positive correlation between these variables. Subsequently, a linear regression equation ($y = k \times x + b$) was fitted to show that the RL intensity of the $Cs_2AgIn_{0.9}Bi_{0.1}Cl_6$/PMMA CFs and radiation dose rate exhibited a good linear relationship ($y = 14.2763 \times x + 1.7545$) (Figure 4e), which highlighted their excellent radiation detection capability.[43] The low dose rate of X-rays can reduce damage to human tissue during medical imaging; thus, the limit of detection (LOD) of scintillator materials for X-rays should be as low as possible for practical applications. According to the International Union of Pure and Applied Chemistry (IUPAC) definition of LOD (signal-to-noise ratio (SNR) is 3:1),[44] the LOD of the $Cs_2AgIn_{0.9}Bi_{0.1}Cl_6$/PMMA CFs—87 $nGy_{air}s^{-1}$ (Figure 4e)—was lower than the typical medical X-ray imaging dose (5.5 $\mu Gy_{air}s^{-1}$).[45] The assessment of a series of optical properties of $Cs_2AgIn_{0.9}Bi_{0.1}Cl_6$/PMMA CFs under X-ray excitation showed that they are suitable for the detection and imaging of X-rays at low doses, which significantly enhances the competitiveness of subsequent developments in the biological field. Finally, a comparison of the light output
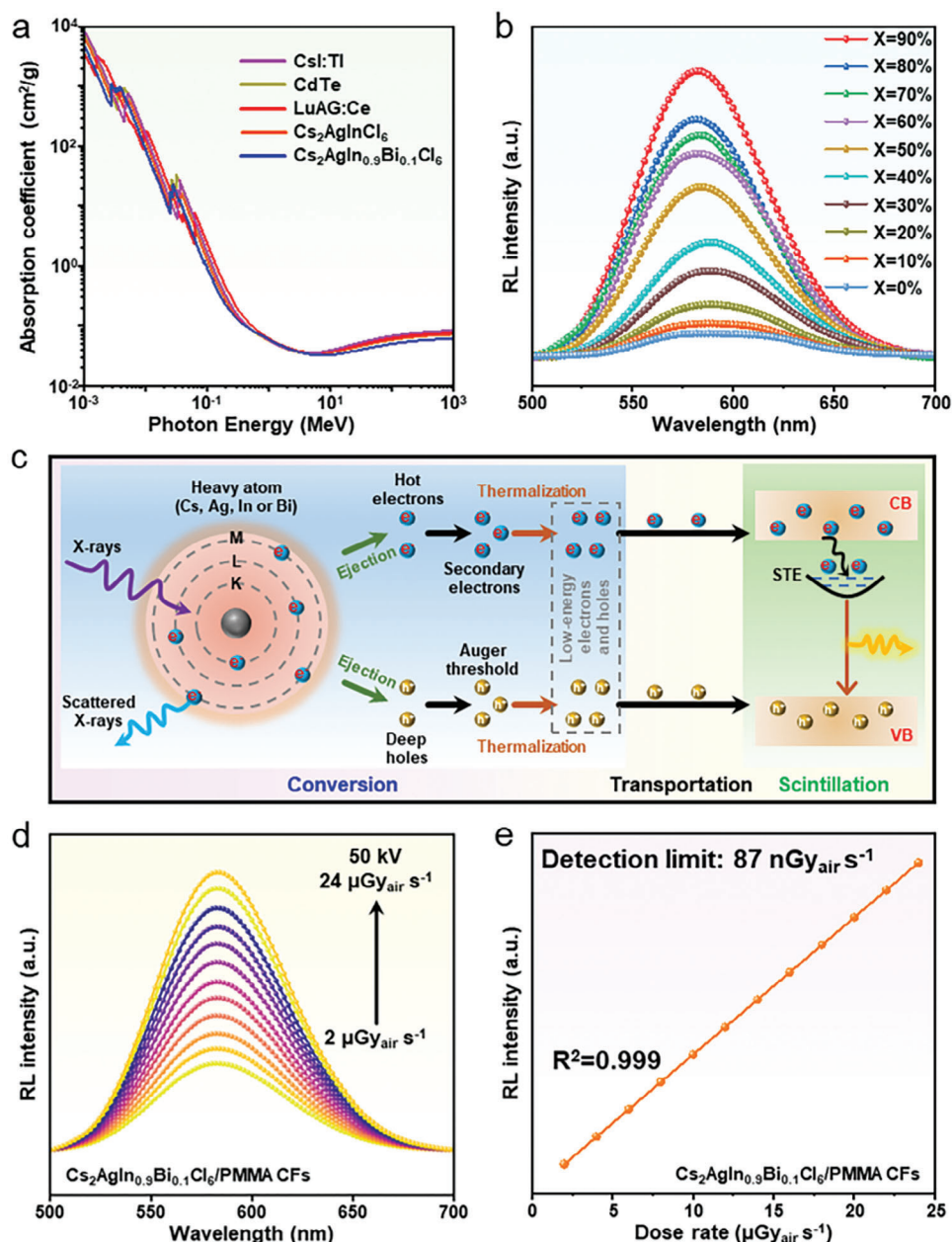
**ADVANCED
SCIENCE NEWS**

www.advancedsciencenews.com

**ADVANCED
OPTICAL
MATERIALS**

www.advopticalmat.de

Figure 4. a) Absorption coefficient of CsI:Tl, CdTe, LuAG:Ce, $Cs_2AgInCl_6$, and $Cs_2AgIn_{0.9}Bi_{0.1}Cl_6$ versus photon energy (MeV). b) RL spectra of $Cs_2AgIn_xBi_{1-x}Cl_6$/PMMA CFs with varying In^{3+} contents at a dose rate of 20 $\mu Gy_{air} s^{-1}$. c) Schematic of the scintillation process in the $Cs_2AgIn_xBi_{1-x}Cl_6$ scintillator. d) RL spectra of the $Cs_2AgIn_{0.9}Bi_{0.1}Cl_6$/PMMA CFs under varying dose rates of X-rays. e) Dose rate versus RL intensity of $Cs_2AgIn_{0.9}Bi_{0.1}Cl_6$/PMMA CFs showing linear relationship for calculating LOD.

and preparation method with other perovskite scintillator films (Table S2, Supporting Information) showed that the in situ-grown $Cs_2AgIn_{0.9}Bi_{0.1}Cl_6$/PMMA CFs exhibited excellent scintillation performances, and the preparation process was significantly optimized.

In practice, the transparency of the scintillation film significantly influences the quality of X-ray imaging.[30] Thinner scintillation films have a higher transmittance and a low concentration of scintillator material, which may not fully absorb X-rays. Conversely, a thicker scintillation film can absorb more

photons, which produces more visible photons owing to the increased interaction of X-rays with atoms, thereby improving the image contrast. However, excessive thickness can limit light penetration and reduce image quality. Therefore, optimizing the transmittance of scintillator films to obtain the best imaging quality is crucial, and this requirement has been reported in many previous studies.[22,30] The in situ fabrication method provided in this study could conveniently control the transmittance of $Cs_2AgIn_{0.9}Bi_{0.1}Cl_6$/PMMA CFs by adjusting the ratio of inorganic material to polymer PMMA in the precursor, thus
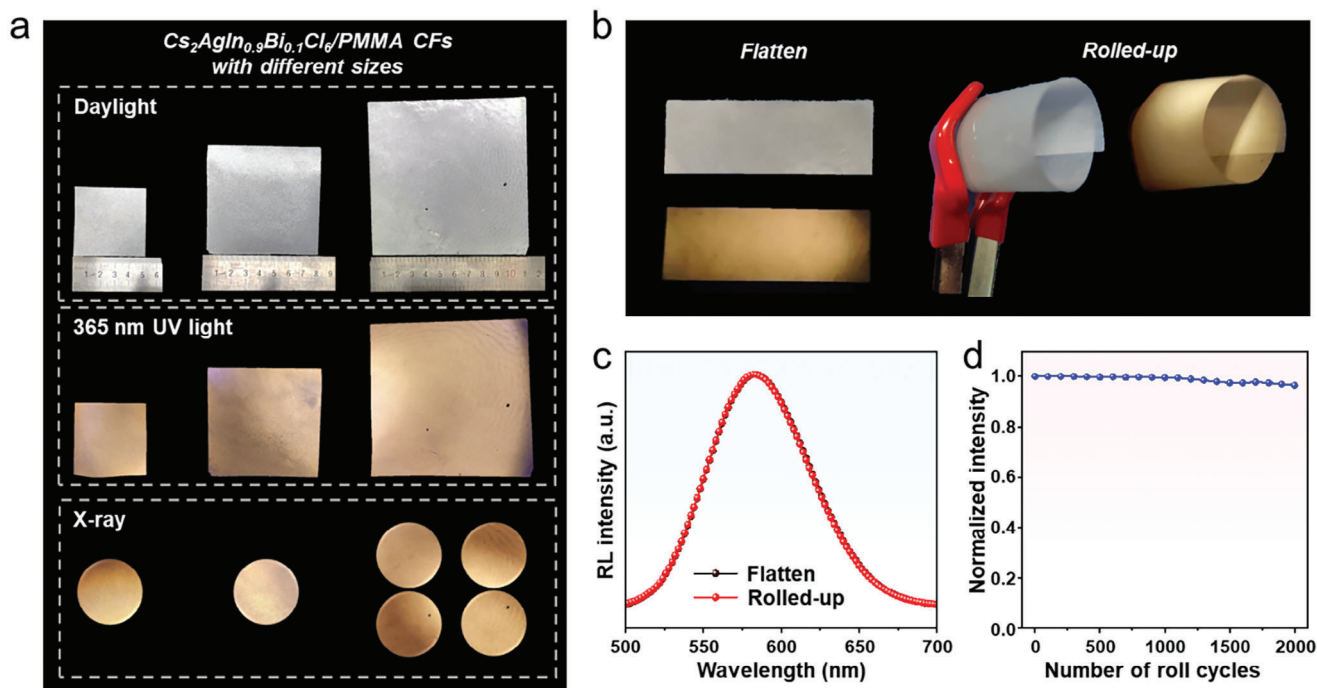
**ADVANCED
SCIENCE NEWS**

www.advancedsciencenews.com

**ADVANCED
OPTICAL
MATERIALS**

www.advopticalmat.de

Figure 5. a) Images of $Cs_2AgIn_{0.9}Bi_{0.1}Cl_6$/PMMA CFs with varying sizes under daylight, 365 nm UV light, and X-ray irradiation. b) Images of flattened and rolled $Cs_2AgIn_{0.9}Bi_{0.1}Cl_6$/PMMA CFs under sunlight and X-ray irradiation. c) RL spectra of flattened and rolled CFs, and d) a normalized RL intensity variation of CFs under a varying number of roll cycles.

yielding four different transmittances of the CFs (T1, T2, T3, and T4) (Figure S8). The radiation logo at the bottom was visible through each CF under daylight; however, its visibility decreased as the $Cs_2AgIn_{0.9}Bi_{0.1}Cl_6$ content increased (Figure S8a, Supporting Information), and the corresponding transmittance decreased from 88% to 12% (Figure S8b, Supporting Information). Finally, the image quality of the $Cs_2AgIn_{0.9}Bi_{0.1}Cl_6$/PMMA CFs with varying transmittance values was assessed using X-ray imaging (Figure S8c, Supporting Information). The image of T2 was the clearest, indicating that the spatial resolution was as high as 12 lp mm^{-1}, and the spatial resolution of the films with other transmittance values was reduced (Figure S8d, Supporting Information). Subsequently, the spatial resolution of $Cs_2AgIn_{0.9}Bi_{0.1}Cl_6$/PMMA CFs with varying transmittance values was quantified using the modulation transfer function (MTF) (Figure S9, Supporting Information), and the MTFs of different samples (the spatial frequency value in line pairs (lp) mm^{-1}@MTF = 0.2) were measured using the slanted edge method. The results were similar to those of the line-pair cards. The above results indicate that the $Cs_2AgIn_{0.9}Bi_{0.1}Cl_6$/PMMA CFs with 66% transmittance were more suitable for X-ray imaging; these CFs were selected for subsequent studies.

Large films are required for practical scintillation applications, and the traditional technology for obtaining scintillator films involves mixing the ground scintillator material and dissolved polymer.[46,47] However, traditional technology is tedious and unsuitable for large-scale preparation, resulting in suboptimal film uniformity. The in situ fabrication strategy proposed in this study can simplify the production process and produce large and uniform scintillator films, which would facilitate subsequent com-

mercialization. $Cs_2AgIn_{0.9}Bi_{0.1}Cl_6$/PMMA CFs of varying sizes (5 × 5, 8 × 8, and 11 × 11 cm^2) were obtained by controlling the size of the blade coater (**Figure 5a**); the $Cs_2AgIn_{0.9}Bi_{0.1}Cl_6$ within the CFs was distributed uniformly, and the surface of the film was smooth, which was crucial for the clarity of the subsequent X-ray image. A uniform orange light was emitted across images of $Cs_2AgIn_{0.9}Bi_{0.1}Cl_6$/PMMA CFs of varying sizes under 365 nm UV irradiation (Figure 5a). This indicated that the applicability of the in situ fabrication method was universal, thereby facilitating the preparation of large $Cs_2AgIn_{0.9}Bi_{0.1}Cl_6$/PMMA CFs. Owing to the limited spot size of the X-rays, different scintillation images were obtained from four positions on the large (11 × 11 cm^2) $Cs_2AgIn_{0.9}Bi_{0.1}Cl_6$/PMMA CFs. In general, the intensity of the scintillation light was unchanged for $Cs_2AgIn_{0.9}Bi_{0.1}Cl_6$/PMMA CFs of varying sizes and positions (Figure 5a), confirming the ability of large CFs to be used for X-ray imaging with large objects. Furthermore, scintillator films with excellent flexibility and stability are frequently required in X-ray detection and imaging applications; therefore, the mechanical stability of $Cs_2AgIn_{0.9}Bi_{0.1}Cl_6$/PMMA CFs was explored. Flexibility was assessed by repeatedly flattening and rolling the film; $Cs_2AgIn_{0.9}Bi_{0.1}Cl_6$/PMMA CFs maintained their structural integrity without any visible cracks or degradation across different mechanical states (Figure 5b). This excellent flexibility suggested that CFs could be applied to flexible wearable and electronic devices. The $Cs_2AgIn_{0.9}Bi_{0.1}Cl_6$/PMMA CFs emitted uniform orange lights under X-ray irradiation in the flattened and rolled conditions (Figure 5b). Additionally, their RL intensity remained consistent before and after rolling (Figure 5c), indicating that the mechanical transformation of the CFs did not affect the
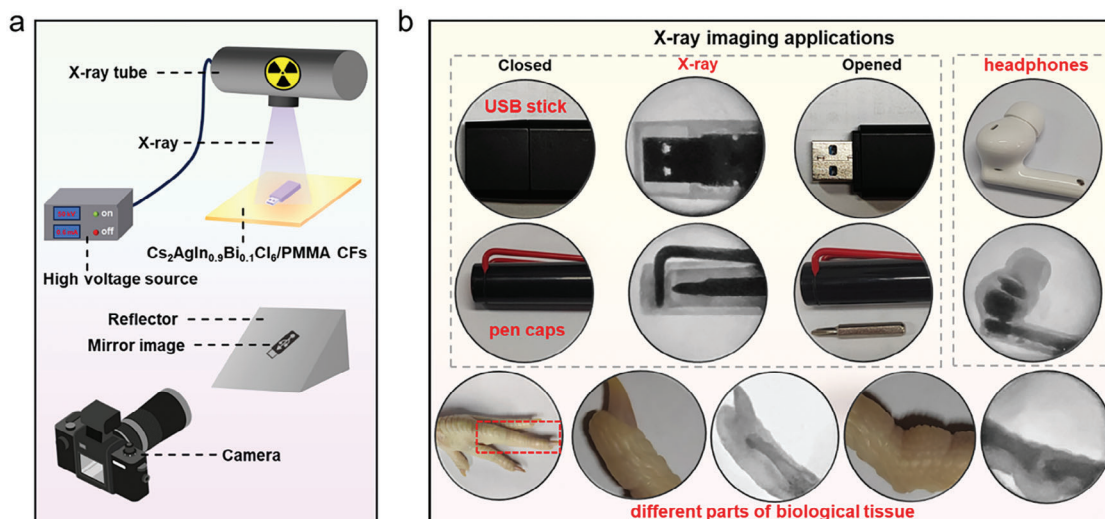
Figure 6. a) Schematic of the X-ray imaging system. b) X-ray imaging of a USB stick, pen caps, headphones, and biological tissues.

RL properties. Subsequently, the damage to the RL intensity of the $Cs_2AgIn_{0.9}Bi_{0.1}Cl_6$/PMMA CFs after multiple rolling cycles was limited (Figure 5d), demonstrating that the CFs had long-term durability and reliability, and were better suited to the demands of the modern commercial market.

Finally, the application of the $Cs_2AgIn_{0.9}Bi_{0.1}Cl_6$/PMMA CFs in actual imaging was evaluated using a homemade X-ray imaging system. The X-ray emission and image collection paths were positioned at 90° in the imaging system, which provided significant protection for the commercial camera, resulting in the collection of mirrored X-ray images (**Figure 6a**). Subsequently, X-ray imaging demonstrations were performed on various objects, such as USB sticks, pen caps, headphones, and commercially available poultry claws, which contain opaque skin, connective tissue, and bone, to simulate medical X-ray imaging scenarios (Figure 6b). For the abiotic samples, the internal metallic components were not visible in daylight (Figure 6b, closed); however, high-resolution and high-contrast internal structural images were obtained under X-ray irradiation (Figure 6b and X-ray), which matched their open images (Figure 6b, open). This phenomenon was attributed to the difference in X-ray absorption between the plastic casing and the metal inside the object, which facilitated the capture of a clear image of the internal metal structure under X-ray irradiation. The scintillator film ($Cs_2AgIn_{0.9}Bi_{0.1}Cl_6$/PMMA CFs) transformed the X-ray light into visible light, which captured the outline of the metal structure. There was a distinct contrast in biological tissues under X-rays; additionally, the joint contours were visible, confirming the potential for $Cs_2AgIn_{0.9}Bi_{0.1}Cl_6$/PMMA CFs in the field of medical imaging. The mentioned practical applications show that $Cs_2AgIn_{0.9}Bi_{0.1}Cl_6$/PMMA CFs can be used for nondestructive imaging of internal structures and advanced fields such as medical imaging and security detection.

3. Conclusion

A method for fabricating large $Cs_2AgIn_xBi_{1-x}Cl_6$/PMMA CFs through the in situ growth of $Cs_2AgIn_xBi_{1-x}Cl_6$ MSs within PMMA was proposed. This method was more convenient and consumed less energy. $Cs_2AgIn_{0.9}Bi_{0.1}Cl_6$/PMMA CFs that exhibited excellent optical properties were prepared by adjusting the In^{3+}/Bi^{3+} ratio to effectively break the forbidden transition. The results demonstrated that $Cs_2AgIn_{0.9}Bi_{0.1}Cl_6$/PMMA CFs possessed outstanding scintillation performance, achieving a light yield of 32000 photons per MeV and an X-ray detection limit of 87 $nGy_{airs}{}^{-1}$. Moreover, these CFs displayed excellent flexibility under X-ray irradiation, and their controlled size was suitable for large-scale industrial production, facilitating their commercialization. Most importantly, $Cs_2AgIn_{0.9}Bi_{0.1}Cl_6$/PMMA CFs exhibited superior performance in X-ray imaging and were capable of achieving high-resolution structural imaging. Consequently, this in situ synthesis strategy can significantly contribute to the development of Pb-free DP scintillator films and has the potential for future applications in medical imaging and security detection.

Supporting Information

Supporting Information is available from the Wiley Online Library or from the author.

Conflict of Interest

The authors declare no conflict of interest.

[1] T. Y. He, Y. Zhou, P. Yuan, J. Yin, L. Gutierrez-Arzaluz, S. L. Chen, J. X. Wang, S. Thomas, H. N. Alshareef, O. M. Bakr, O. F. Mohammed, *ACS Energy Lett.* **2023**, *8*, 1362.

[2] B. H. Li, Y. Xu, X. L. Zhang, K. Han, J. C. Jin, Z. G. Xia, *Adv. Opt. Mater.* **2022**, *10*, 2102793.

[3] Q. S. Chen, J. Wu, X. Y. Ou, B. L. Huang, J. Almutlaq, A. A. Zhumekenov, X. W. Guan, S. Y. Han, L. L. Liang, Z. G. Yi, J. Li, X. J. Xie, Y. Wang, Y. Li, D. Y. Fan, D. B. L. Teh, A. H. All, O. F. Mohammed, O. M. Bakr, T. Wu, M. Bettinelli, H. H. Yang, W. Huang, X. G. Liu, *Nature.* **2018**, *561*, 88.

[4] D. J. Yu, P. Wang, F. Cao, Y. Gu, J. X. Liu, Z. Y. Han, B. Huang, Y. S. Zou, X. B. Xu, H. B. Zeng, *Nat. Commun.* **2020**, *11*, 3395.

[5] J. Perego, I. Villa, A. Pedrini, E. C. Padovani, R. Crapanzano, A. Vedda, C. Dujardin, C. X. Bezuidenhout, S. Bracco, P. E. Sozzani, A. Comotti, L. Gironi, M. Beretta, M. Salomoni, N. Kratochwil, S. Gundacker, E. Auffray, F. Meinardi, A. Monguzzi, *Nat. Photonics.* **2021**, *15*, 393.

[6] C. Roques-Carmes, N. Rivera, A. Ghorashi, S. E. Kooi, Y. Yang, Z. Lin, J. Beroz, A. Massuda, J. Sloan, N. Romeo, Y. Yu, J. D. Joannopoulos, I. Kaminer, S. G. Johnson, M. Soljacic, *Science.* **2022**, *375*, 837.

[7] X. M. Liu, Y. Y. Jiang, F. Y. Li, X. L. Xu, R. H. Li, W. J. Zhu, J. F. Ni, C. B. Ding, S. J. Liu, Q. Zhao, *Adv. Opt. Mater.* **2023**, *11*, 2202169.

[8] A. Jana, S. Cho, S. A. Patil, A. Meena, Y. Jo, V. G. Sree, Y. Park, H. Kim, H. Im, R. A. Taylor, *Mater. Today* **2022**, *55*, 110.

[9] J. B. Luo, J. H. Wei, Z. Z. Zhang, Z. L. He, D. B. Kuang, *Angew. Chem. Int. Ed.* **2023**, *62*, 2216504.

[10] H. T. Wei, D. DeSantis, W. Wei, Y. H. Deng, D. Y. Guo, T. J. Savenije, L. Cao, J. S. Huang, *Nat. Mater.* **2017**, *16*, 826.

[11] G. Kakavelakis, M. Gedda, A. Panagiotopoulos, E. Kymakis, T. D. Anthopoulos, K. Petridis, *Adv. Sci.* **2020**, *7*, 2002098.

[12] W. Zhao, G. Ristic, J. A. Rowlands, *Med. Phys.* **2004**, *31*, 2594.

[13] J. J. Zhao, L. Zhao, Y. H. Deng, X. Xiao, Z. Y. Ni, S. Xu, J. S. Huang, *Nat. Photonics.* **2020**, *14*, 612.

[14] H. X. Meng, W. J. Zhu, Z. J. Zhou, R. Y. Zhou, D. Yan, Q. Zhao, S. J. Liu, *J. Mater. Chem. C.* **2022**, *10*, 12286.

[15] J. D. Shi, Z. Y. Wang, N. V. Gaponenko, Z. Da, C. Zhang, J. N. Wang, Y. Q. Ji, Y. S. Ding, Q. Yao, Y. L. Xu, M. Q. Wang, *Small.* **2024**, 2310478.

[16] H. D. Tang, Y. Q. Xu, X. B. Hu, Q. Hu, T. Chen, W. H. Jiang, L. J. Wang, W. Jiang, *Adv. Sci.* **2021**, *8*, 2004118.

[17] J. D. Shi, M. Q. Wang, C. Zhang, J. N. Wang, Y. Zhou, Y. L. Xu, N. V. Gaponenko, A. S. Bhatti, *ACS Appl. Mater. Interfaces.* **2023**, *15*, 12383.

[18] J. D. Shi, Z. Y. Wang, N. Gaponenko, Z. Da, C. Zhang, J. N. Wang, Y. Q. Ji, Q. Yao, Y. S. Ding, M. Q. Wang, Y. L. Xu, *Mater. Today Chem.* **2024**, *35*, 101874.

[19] T. Cai, W. W. Shi, S. Hwang, K. Kobbekaduwa, Y. Nagaoka, H. J. Yang, K. Hills-Kimball, H. Zhu, J. Y. Wang, Z. G. Wang, Y. Z. Liu, D. Su, J. B. Gao, O. Chen, *J. Am. Chem. Soc.* **2020**, *142*, 11927.

[20] S. L. Jin, R. F. Li, H. Huang, N. Z. Jiang, J. D. Lin, S. X. Wang, Y. H. Zheng, X. Y. Chen, D. Q. Chen, *Light Sci. Appl.* **2022**, *11*, 52.

[21] N. Zhang, R. Zhang, X. M. Xu, F. Wang, Z. C. Sun, S. H. Wang, S. F. Wu, *Adv. Opt. Mater.* **2023**, *11*, 2300187.

[22] N. Varnakavi, R. Rajavaram, K. Gupta, P. R. Cha, N. Lee, *Adv. Opt. Mater.* **2024**, *12*, 2301868.

[23] Z. Y. Xu, X. Liu, Y. B. Li, X. T. Liu, T. Yang, C. M. Ji, S. G. Han, Y. D. Xu, J. H. Luo, Z. H. Sun, *Angew. Chem. Int. Ed.* **2019**, *58*, 15757.

[24] N. K. Tailor, J. Ghosh, M. A. Afroz, S. Bennett, M. Chatterjee, P. Sellin, S. Satapathi, *ACS Appl. Electron. Mater.* **2022**, *4*, 4530.

[25] C. F. Wang, H. J. Li, M. G. Li, Y. Cui, X. Son, Q. W. Wang, J. Y. Jiang, M. M. Hua, Q. Xu, K. Zhao, H. Y. Ye, Y. Zhang, *Adv. Funct. Mater.* **2021**, *31*, 2009457.

[26] W. J. Zhu, W. B. Ma, Y. R. Su, Z. Chen, X. Y. Chen, Y. G. Ma, L. Z. Bai, W. G. Xiao, T. Y. Liu, H. M. Zhu, X. F. Liu, H. F. Liu, X. Liu, Y. Yang, *Light Sci. Appl.* **2020**, *9*, 112.

[27] Z. Y. Wang, J. S. Chen, X. Xu, T. X. Bai, Q. K. Kong, H. Yin, Y. Yang, W. W. Yu, R. L. Zhang, X. J. Liu, K. L. Han, *Adv. Opt. Mater.* **2024**, *12*, 2302617.

[28] C. Wang, J. W. Xiao, Z. G. Yan, X. W. Niu, T. F. Lin, Y. C. Zhou, J. Y. Li, X. D. Han, *Nano Res.* **2023**, *16*, 1703.

[29] F. Maddalena, M. E. Witkowski, M. Makowski, A. Bachiri, Arramel, T. Y., M. H. Mahyuddin, M. Baravaglio, M. Boutchich, W. Drozdowski, C. Dujardin, M. D. Birowosuto, C. Dang, *J. Mater. Chem. C.* **2022**, *10*, 11266.

[30] Y. Y. Liu, K. Han, S. H. Zhao, X. Q. Zhou, S. Gao, Y. X. Wang, Z. G. Xia, S. D. Jiang, *J. Mater. Chem. C.* **2024**, *12*, 3221.

[31] J. D. Shi, M. Q. Wang, C. Zhang, J. N. Wang, Y. Zhou, Y. L. Xu, N. V. Gaponenko, *Mater. Today Chem.* **2023**, *29*, 101480.

[32] J. D. Shi, M. Q. Wang, C. Zhang, J. N. Wang, Y. Zhou, Y. L. Xu, N. V. Gaponenko, *J. Mater. Chem. C.* **2023**, *11*, 4742.

[33] W. W. Meng, X. M. Wang, Z. W. Xiao, J. B. Wang, D. B. Mitzi, Y. F. Yan, *J. Phys. Chem. Lett.* **2017**, *8*, 2999.

[34] B. Yang, X. Mao, F. Hong, W. W. Meng, Y. X. Tang, X. S. Xia, S. Q. Yang, W. Q. Deng, K. L. Han, *J. Am. Chem. Soc.* **2018**, *140*, 17001.

[35] H. Arfin, A. S. Kshirsagar, J. Kaur, B. Mondal, Z. G. Xia, S. Chakraborty, A. Nag, *Chem. Mater.* **2020**, *32*, 10255.

[36] J. D. Majher, M. B. Gray, T. A. Strom, P. M. Woodward, *Chem. Mater.* **2019**, *31*, 1738.

[37] S. Li, H. Y. Wang, P. Yang, L. L. Wang, X. R. Cheng, K. Yang, *J. Alloy Compd.* **2021**, *854*, 156930.

[38] G. Y. Zhang, D. Y. Wang, B. B. Lou, C. G. Ma, A. Meijerink, Y. H. Wang, *Angew. Chem. Int. Ed.* **2022**, *61*, 2022074.

[39] P. Han, X. Mao, S. Yang, F. Zhang, B. Yang, D. Wei, W. Deng, K. Han, *Angew. Chem. Int. Ed.* **2019**, *58*, 17231.

[40] B. A. Connor, L. Leppert, M. D. Smith, J. B. Neaton, H. I. Karunadasa, *J. Am. Chem. Soc.* **2018**, *140*, 5235.

[41] J. D. Shi, W. Y. Ge, Y. Tian, M. M. Xu, W. X. Gao, Y. T. Wu, *Small.* **2021**, *17*, 2006568.

[42] D. Shi, V. Adinolfi, R. Comin, M. J. Yuan, E. Alarousu, A. Buin, Y. Chen, S. Hoogland, A. Rothenberger, K. Katsiev, Y. Losovyj, X. Zhang, P. A. Dowben, O. F. Mohammed, E. H. Sargent, O. M. Bakr, *Science.* **2015**, *347*, 519.

[43] J. H. Han, T. Samanta, Y. M. Park, H. J. Kim, N. S. M. Viswanath, H. W. Kim, B. K. Cha, S. B. Cho, W. B. Im, *ACS Energy Lett.* **2023**, *8*, 545.

[44] B. Yang, L. X. Yin, G. D. Niu, J. H. Yuan, K. H. Xue, Z. F. Tan, X. S. Miao, M. Niu, X. Y. Du, H. S. Song, E. Lifshitz, J. Tang, *Adv. Mater.* **2019**, *31*, 1904711.

[45] H. T. Wei, Y. J. Fang, P. Mulligan, W. Chuirazzi, H. H. Fang, C. C. Wang, B. R. Ecker, Y. L. Gao, M. A. Loi, L. Cao, J. S. Huang, *Nat. Photonics.* **2016**, *10*, 333.

[46] Y. H. Zhang, R. J. Sun, X. Y. Qi, K. F. Fu, Q. S. Chen, Y. C. Ding, L. J. Xu, L. M. Liu, Y. Han, A. V. Malko, X. G. Liu, H. H. Yang, O. M. Bakr, H. Liu, O. F. Mohammed, *ACS Nano.* **2019**, *13*, 2520.

[47] B. Q. Wang, J. L. Peng, X. Yang, W. S. Cai, H. B. Xiao, S. Y. Zhao, Q. Q. Lin, Z. G. Zang, *Laser Photonics Rev.* **2022**, *16*, 210073.